

Embracing Events and Frames with Hierarchical Feature Refinement Network for Object Detection

Hu Cao¹, Zehua Zhang¹, Yan Xia^{1,4}, Xinyi Li¹, Jiahao Xia², Guang Chen^{3*}, and Alois Knoll¹

¹ Technical University of Munich, Munich, Germany
{hu.cao,zehua.zhang,yan.xia,super.xinyi,k}@tum.de

² University of Technology Sydney, Sydney, Australia
Jiahao.Xia@student.uts.edu.au

³ Tongji University, Shanghai, China
guangchen@tongji.edu.cn

⁴ Munich Center for Machine Learning (MCML)

Abstract. In frame-based vision, object detection faces substantial performance degradation under challenging conditions due to the limited sensing capability of conventional cameras. Event cameras output sparse and asynchronous events, providing a potential solution to solve these problems. However, effectively fusing two heterogeneous modalities remains an open issue. In this work, we propose a novel hierarchical feature refinement network for event-frame fusion. The core concept is the design of the coarse-to-fine fusion module, denoted as the cross-modality adaptive feature refinement (CAFR) module. In the initial phase, the bidirectional cross-modality interaction (BCI) part facilitates information bridging from two distinct sources. Subsequently, the features are further refined by aligning the channel-level mean and variance in the two-fold adaptive feature refinement (TAFR) part. We conducted extensive experiments on two benchmarks: the low-resolution PKU-DDD17-Car dataset and the high-resolution DSEC dataset. Experimental results show that our method surpasses the state-of-the-art by an impressive margin of **8.0%** on the DSEC dataset. Besides, our method exhibits significantly better robustness (**69.5%** versus **38.7%**) when introducing 15 different corruption types to the frame images. The code can be found at the link (<https://github.com/HuCaoFighting/FRN>).

Keywords: Event camera · Multi-sensor fusion · Object detection

1 Introduction

Object detection is a fundamental task in computer vision [9, 32, 39]. The performance of conventional frame-based cameras in object detection often faces a significant decline in challenging conditions, such as high-speed motion, poor lighting conditions (e.g. low-light and overexposure), and image corruptions [21,

* Corresponding author

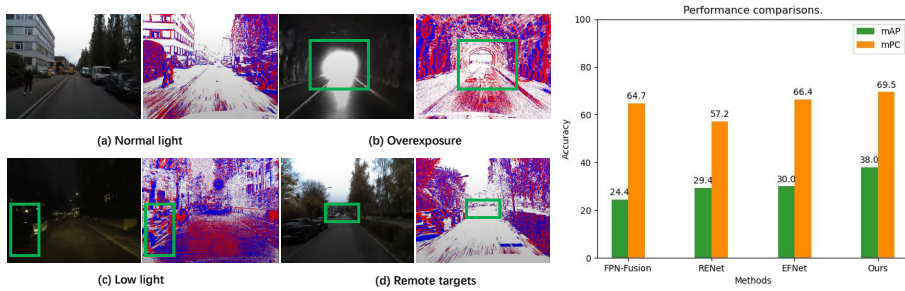


Fig. 1: This work leverages the complementary information from both events and frames for object detection. (Left) In each image pair, the left image is from frames, while the right is from events. Note that event cameras excel at high-speed and high-dynamic range sensing but struggle to capture static and remote small targets compared to RGB cameras. (Right) We choose three methods, FPN-Fusion [48], RENet [58], and EFNet [46] for performance evaluation.

36, 45]. Recently, an emerging bio-inspired vision sensor, the event camera (e.g., dynamic and active pixel vision sensors, DAVIS), has been developed for vision perception [3, 37]. The working principle of the event camera fundamentally differs from that of the conventional camera. It transmits only the local pixel-level changes caused by variations in lighting intensity, like a bio-inspired retina [7, 14]. The event camera has several appealing characteristics, including low latency, high dynamic range (120 dB), and high temporal resolution. It offers a new perspective to address some limitations of conventional cameras in challenging scenarios. However, similar to the problems faced by conventional cameras in extreme-light scenarios, event cameras exhibit poor performance in static or remote scenes with small targets, as illustrated in Fig. 1. The event camera captures dynamic context and structural information, whereas the frame-based camera provides rich color and texture information. Both event cameras and frame-based cameras are complementary, motivating the development of new algorithms for various computer vision tasks.

Current event-frame fusion methods often utilize concatenation [4, 48], attention mechanisms [5, 46, 58], and post-processing [8, 24, 27] strategies to fuse events and frames. Simply concatenating event-based and frame-based features improves performance slightly, but the inherent complementary nature between different modalities is not fully exploited. The authors of [5] employ pixel-level spatial attention to leverage event-based features in enhancing frame-based features, leading to improved performance. However, enhancing single-modal features is considered suboptimal, as event-based features and frame-based features possess unique characteristics. The methods presented in [46, 58] incorporate feature interaction between event-based and frame-based features; however, they do not comprehensively consider the feature imbalance problems existing in event-frame object detection. As illustrated in Fig. 2, we present the feature maps before and after the application of our fusion module. In the daytime scene,



Fig. 2: Feature maps of RGB and event modalities before and after CAFR. The first row corresponds to the day scene, and the last row represents the night scene.

event-based features struggle to effectively capture the remote car compared to RGB-based features. Conversely, in the night scene, RGB-based features face challenges in capturing cars effectively compared to event-based features due to lighting conditions. The feature-modality imbalance problem stems from the misalignment and inadequate integration of different modalities. Addressing this issue requires fully incorporating cross-modal complementarity to generate robust features.

To address the aforementioned problems, we propose a novel hierarchical feature refinement network with CAFR modules for event-frame fusion. In contrast to the current event-frame fusion methods, our method adopts a dual-branched coarse-to-fine structure. The dual-branch architecture guarantees comprehensive utilization of both event-based and frame-based features. To extract refined features, following the initial feature interaction, we further employ feature statistics to align features at the channel-level mean and variance, thereby enhancing the model’s representation capabilities. Specifically, CAFR consists of two parts: the bidirectional cross-modality interaction (BCI) part and the two-fold adaptive feature refinement (TAFR) part, where attention mechanisms and feature statistics are utilized to balance feature representations. Extensive experiments demonstrate that our method outperforms the state-of-the-art (SOTA) on several datasets (PKU-DDD17-Car, DSEC, and corruption data).

The main contributions of this work can be summarized as follows:

- We propose a novel hierarchical feature refinement network with CAFR modules to fuse events and frames, which enriches extracted features with more valuable information, thereby enhancing the overall detection performance.
- BCI and TAFR parts are devised to constitute the CAFR by incorporating sufficiently complementary information to form discriminative representations for robust object detection.

- Our method outperforms SOTA methods on the low-resolution PKU-DDD17-Car dataset, the high-resolution DSEC dataset, and the corruption data. As shown in Fig. 1, our model outperforms the second-best model, EFNet [46], by an impressive margin of **8.0%** mAP and **3.1%** mPC, respectively.

2 Related Work

Event-based object detection. Several event-based detection methods, such as RED [41], ASTMNet [28], and RVT [17], leverage the remarkable capabilities of event cameras. RED [41] introduces a ConvLSTM recurrent network architecture for extracting spatio-temporal features from event streams. Similarly, ASTMNet [28] introduces a spatio-temporal attentional convolution module for learning event feature embeddings, alongside a lightweight spatio-temporal memory module for extracting cues from continuous event streams. On the other hand, RVT [17] proposes a pioneering backbone algorithm for object detection, substantially reducing inference time while maintaining performance levels comparable to previous methods. Nevertheless, the absence of color and fine-grained texture details in event streams results in insufficient semantic information, which is crucial for effective detection tasks.

Event-frame fusion for object detection. In the field of object detection, the authors of [27] and [8] adopt the Dempster-Shafer theory to fuse events and frames for vehicle detection and pedestrian detection, respectively. Additionally, Chen et al. [10] employ non-maximum suppression (NMS) for fusing the detection outcomes of two modalities, while Jiang et al. [24] suggest fusing confidence maps derived from the two modalities. All the above methods can be categorized as late fusion methods. While late fusion can be effective, these methods often lack feature interactions and struggle to fully exploit the complementary nature of the fused modalities. Recently, various middle fusion methods [5, 48, 58] have been proposed to guide the fusion of two modalities at the feature level. In [4, 48], simple concatenation is employed to fuse event-based and frame-based features for performance improvement. The authors of [5] utilize pixel-level spatial attention to leverage event-based features for enhancing frame-based features, resulting in improved performance. However, due to the uniqueness of event-based features and frame-based features, enhancing single-mode features is considered suboptimal. The approach introduced in [58] incorporates feature interaction between event-based and frame-based features, but they do not fully address the feature imbalance issues present in event-frame object detection.

Various fusion modules for events and frames. Multimodal fusion methods for events and frames have been explored across various vision tasks, including deblurring [46], steering angle prediction [38], depth estimation [15], and semantic segmentation [55]. In [46], the cross-self-attention is proposed as a fusion module to combine events and frames to improve deblurring performance. In contrast, the authors of [38] processed events and frames separately with the self-attention module and then summed the outputs to get the fusion features. For depth estimation, RAM Net is developed in [38] to leverage events and

frames’ information. Moreover, a unified fusion framework, CMX, is introduced in [55] for RGB-X semantic segmentation.

3 Method

In this section, we first introduce preliminaries, including the working principles of the event camera and event representation. Subsequently, we delve into a detailed illustration of our proposed hierarchical feature refinement network.

3.1 Preliminaries

Event camera. The conventional frame-based camera operates by capturing and delivering a sequence of frames at a fixed frequency. In stark contrast, the working principle of the event camera deviates fundamentally from that of its frame-based counterpart. The event camera, a bio-inspired vision sensor, generates asynchronous and sparse event streams exclusively when the change in logarithmic intensity $L(x, y, t)$ surpasses a predetermined threshold C . The computational process can be succinctly formulated as follows:

$$L(x, y, t) - L(x, y, t - \Delta t) \geq pC, \quad p \in \{-1, +1\}. \quad (1)$$

where Δt represents the time variation. The event polarity, denoted by $p \in \{-1, +1\}$, signifies the sign of the brightness change, indicating either positive (“ON”) or negative (“OFF”) events, respectively. The generated event streams E can be expressed as follows:

$$E = \{e_i\}_{i=1}^N, e_i = (x_i, y_i, t_i, p_i). \quad (2)$$

where N denotes the number of events e_i within the event stream E . The tuple (x, y) denotes the triggered pixel coordinates, while t and p represent the corresponding timestamp and polarity, respectively.

Event representation. The event representation employed in this study is the voxel grid [59] generated through the discretization of the time domain. Considering a set of N input events $\{(x_i, y_i, t_i, p_i)\}_{i \in [1, N]}$ and a set of B bins for discretizing the time dimension, we normalize the timestamps to the range $[0, B - 1]$. Subsequently, the event volume is generated as follows:

$$t_i^* = \frac{(B - 1)(t_i - t_1)}{t_N - t_1},$$

$$V(x, y, t) = \sum_i p_i k_b(x - x_i) k_b(y - y_i) k_b(t - t_i^*), \quad (3)$$

$$k_b(a) = \max(0, 1 - |a|).$$

where $k_b(a)$ corresponds to the bilinear sampling kernel, as defined in [42]. More specifically, we regard the time domain of the voxel grid as channels in a conventional 2D image and conduct a 2D convolution across the spatial dimensions x and y . This approach enables the model to effectively capture feature representations from the spatiotemporal distribution of events.

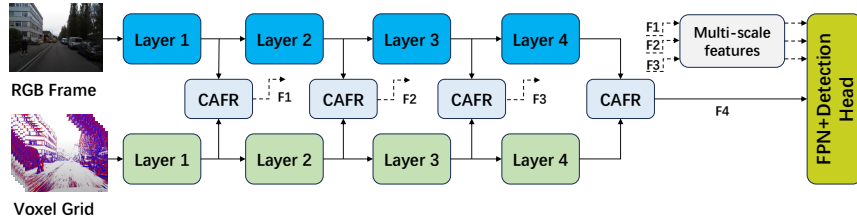


Fig. 3: The overall architecture of our hierarchical feature refinement network. It comprises a dual-stream backbone network, CAFR, FPN, and a detection head. The backbone incorporates two branches: the event-based ResNet-50 (bottom) and the frame-based ResNet-50 [18] (top). The CAFR operates to enhance features on a hierarchical scale. The refined multi-scale features are then forwarded to the FPN and detection head for accurate detection predictions. The structure of the FPN and the detection head is adapted from [30].

3.2 Hierarchical Feature Refinement Network

Overview. The method’s architecture, illustrated in Fig. 3, comprises a dual-stream backbone, CAFR, a feature pyramid network (FPN), and a detection head. Events are preprocessed using the voxel grid encoding method for CNN to extract deep features. Utilizing event-frame data as inputs, the dual-stream backbone network extracts multi-scale features. For effective information exchange between different modal features, CAFR receive event-based and frame-based features to balance the information flow. Subsequently, the detection head operates on the harmonized multi-modal features for precise detection predictions. Detailed explanations of each module will be provided in the subsequent parts.

Dual-stream backbone. The backbone incorporates two branches: event-based and frame-based ResNet-50s [18]. Each ResNet-50 is composed of four blocks denoted as $\{L_1, L_2, L_3, L_4\}$. The feature maps’ resolution progressively decreases from L_1 to L_4 , with the resolution of the features being consistently maintained at each block. Residual learning is employed to extract semantically stronger and more valuable features. In this work, a CAFR module is strategically inserted between the two blocks to enhance the learning process.

Cross-modality adaptive feature refinement (CAFR) module. Frame-based cameras perform poorly in several challenging scenarios, such as overexposure, high-speed motion, etc. Furthermore, frame-based features may generate unclear results because objects share many visual similarities. In contrast, event cameras with high temporal resolution and dynamic range excel at capturing motion and edge information. Recognizing the complementarity of event-based and frame-based information, we introduce the CAFR to enhance feature representations at the feature level by leveraging event-based dynamic context. As depicted in Fig. 4, CAFR processes both frame-based features F_f and event-based features F_e to obtain balanced semantic features.

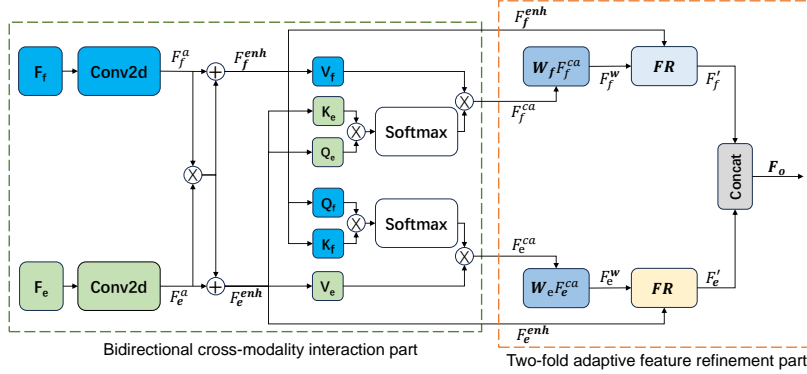


Fig. 4: Cross-modality adaptive feature refinement module (CAFR). It contains two integral parts: bidirectional cross-modality interaction (BCI) and two-fold adaptive feature refinement (TAFR). Here, “FR” denotes feature refinement.

Bidirectional cross-modality interaction (BCI). Initially, a transformation module, utilizing a 1×1 convolution layer, is employed for activation. The calculation can be expressed as follows:

$$F_f^a = \text{Conv}_{1 \times 1}(F_f), F_e^a = \text{Conv}_{1 \times 1}(F_e). \quad (4)$$

Subsequently, the activated frame and event features undergo a coarse-to-fine fusion. Specifically, a global attention map is computed through pixel-wise multiplication, representing mixed attention across spatial and channel dimensions to enhance features. Formally, the computation for enhanced features F_f^{enh} and F_e^{enh} is as follows:

$$F_f^{enh} = F_f^a \otimes F_e^a + F_f^a, F_e^{enh} = F_e^a \otimes F_f^a + F_e^a. \quad (5)$$

To bridge information from two distinct sources, the features undergo processing via a bidirectional cross-self-attention mechanism at a coarse level. The input features F_f^{enh} and F_e^{enh} are first projected into query (Q_f and Q_e), key (K_f and K_e), and value (V_f and V_e) tensors. The computation can be expressed as follows:

$$\begin{aligned} Q_f &= F_f^{enh} W_f^Q, K_f = F_f^{enh} W_f^K, \\ V_f &= F_f^{enh} W_f^V, Q_e = F_e^{enh} W_e^Q, \\ K_e &= F_e^{enh} W_e^K, V_e = F_e^{enh} W_e^V. \end{aligned} \quad (6)$$

where W represents a learnable linear projection.

In contrast to self-attention in [6, 51, 52], which focuses on relationships within an individual feature modality, cross-self-attention extends its scope by incorporating guidance from the counterpart feature modality. This mechanism captures semantics as:

$$F_f^{ca} = CrossAtt_f(Q_e, K_e, V_f), F_e^{ca} = CrossAtt_e(Q_f, K_f, V_e). \quad (7)$$

Where $CrossAtt_f$ is defined as follows:

$$CrossAtt_f(Q_e, K_e, V_f) = SoftMax\left(\frac{Q_e K_e^T}{\sqrt{D}}\right)V_f. \quad (8)$$

where D denotes the channel dimension of the feature map. $CrossAtt_e$ is computed in a similar manner.

Two-fold adaptive feature refinement (TAFR). Furthermore, we employ feature statistics to align the feature space, leveraging insights from the style transfer domain [22]. Specifically, the features undergo further refinement by aligning the channel-level mean and variance. The resulting final output, denoted as F_o , is attained by concatenating the two aligned features. This entire process is represented as follows:

$$\begin{aligned} F_f^w &= W_f F_f^{ca}, & F_e^w &= W_e F_e^{ca}, \\ F_f' &= \frac{\sigma(F_f^{enh})(F_f^w - \mu(F_f^w))}{\sigma(F_f^w)} + \mu(F_f^{enh}), \\ F_e' &= \frac{\sigma(F_e^{enh})(F_e^w - \mu(F_e^w))}{\sigma(F_e^w)} + \mu(F_e^{enh}), \\ F_o &= Concat(F_f', F_e'). \end{aligned} \quad (9)$$

where W_f and W_e represent learnable linear projections. Notably, the computation for F_f' , F_e' , and F_o operates without learnable affine parameters. Instead, it adaptively computes the affine parameters directly from the inputs. The computation of μ and σ is expressed as:

$$\begin{aligned} \mu(x) &= \frac{1}{H \times W} \sum_{h=1}^H \sum_{w=1}^W x, \\ \sigma(x) &= \sqrt{\frac{1}{H \times W} \sum_{h=1}^H \sum_{w=1}^W (x - \mu(x))^2 + \epsilon}. \end{aligned} \quad (10)$$

Where x denotes the input feature maps. H and W represent the height and width of the input feature map, respectively. ϵ is a small value introduced to prevent division by zero, typically set to 1×10^{-5} .

FPN and detection head. Similar to the previous works [5, 29, 30], we employ FPN to enhance features, improving detection robustness for objects of varying sizes. The outputs $\{P_n\}_{n=1}^4$ are generated through top-down pathways and lateral connections. The last level of the feature map, P_5 , is obtained by applying a 3×3 convolutional layer with stride 2 on P_4 . The resulting multi-level feature maps $\{P_n\}_{n=1}^5$ are then fed into the detection head for prediction.

After FPN processing, the detection head comprises two subnets responsible for classification and bounding box regression. Each sub-network comprises four

3×3 convolutional layers with 256 filters. In the classification sub-network, followed by a 3×3 convolutional layer with KA filters, followed by sigmoid activations, it outputs KA binary predictions. In the bounding box regression sub-network, followed by a 3×3 convolutional layer with $4A$ filters, it outputs $4A$ offset predictions. A is set to 9. The specific offset parameters of the bounding box can be expressed as follows:

$$\begin{aligned} t'_x &= \frac{(x' - x_a)}{w_a}, t'_y = \frac{(y' - y_a)}{h_a}, \\ t'_w &= \log\left(\frac{w'}{w_a}\right), \quad t'_h = \log\left(\frac{h'}{h_a}\right). \end{aligned} \tag{11}$$

where x, y, w, h denote the center coordinates, width, and height of the bounding box, respectively. The variables t', x', x_a represent the prediction regression offsets, predicted bounding box, and anchor box, respectively.

4 Experiments

In this section, we outline the datasets and evaluation metrics used for event-frame multimodal object detection. Extensive experiments are then conducted to evaluate the effectiveness of our proposed method.

4.1 Datasets

DDD17. The DDD17 dataset [1] is collected to combine events and frames for end-to-end driving applications. It uses a 346×260 pixel DAVIS to record over 12 hours of highway and city driving in various conditions (daytime, evening, night, dry, etc.). However, the original DDD17 dataset does not have object detection labels. The authors of [27] manually labeled the vehicles in the DDD17 dataset to make them available for object detection tasks, named PKU-DDD17-Car. The PKU-DDD17-Car dataset contains frame data and corresponding event streams, of which 2241 frames are the training set and 913 frames are the test set.

DSEC. DSEC [16] is a high-resolution and large-scale event-frame dataset for real-world driving scenarios. Concurrently, event data is captured using an event camera with a resolution of 640×480 . Unlike the DDD17 dataset, where both event data and frame data originate from the same DAVIS camera, the DSEC dataset features non-synchronized event and RGB data. To address this, a homographic transformation based on camera matrices is employed to align the viewpoint and resolution of the event and RGB cameras. The initial release of the DSEC dataset lacks annotations for object detection. In this study, we utilize the labels introduced in [48] for evaluation. Specifically, the labeled dataset encompasses three object categories: cars, pedestrians, and large vehicles.

Corruption data. Previous studies [12, 36, 48] indicate significant performance degradation (as low as 30–60% of the original performance) in standard object detection models when applied to corrupted images. To assess model’s robustness, we introduced 15 distinct corruption types to frame images, including gaussian noise, shot noise, impulse noise, defocus blur, frosted glass blur,

Table 1: The performance of different modality inputs on the PKU-DDD17-Car and DSEC datasets.

Method	PKU-DDD17-Car (mAP_{50} %)	DSEC (mAP %)
Events Only	46.5	12.0
Frames Only	82.7	25.0
CAFR (Ours)	86.7	38.0

motion blur, zoom blur, snow, frost, fog, brightness, contrast, elastic, pixelate, and JPEG compression. These corruptions can be broadly categorized into four groups: noise, blur, weather, and digital. Each corruption type is subjected to five severity levels. Please find more details in the **Supplemental material**.

4.2 Evaluation Metrics

We use the widely-adopted mAP metric [31] to evaluate the detection performance of different methods. When assessing performance over corrupted data, we utilize the mean performance under corruption (mPC) metric [19, 36]. This metric represents the average mAP over various corruption types and severity levels, as expressed below:

$$mPC = \frac{1}{N_C} \sum_{c=1}^{N_C} \frac{1}{N_S} \sum_{s=1}^{N_S} mAP_{c,s}. \quad (12)$$

where $mAP_{c,s}$ represents the performance measure evaluated on corruption type c under severity level s , N_c is the number of corruption types (15 in our work), and N_s is the number of severity levels considered (5 in our work).

4.3 Ablation Study

In this section, we conduct a series of ablation experiments to assess the effectiveness of the proposed modules. The results are summarized in Tab. 1 and Tab. 2.

Multi-modal vs. single-modal. In Tab. 1, we compare the performance of different modality inputs. Firstly, RetinaNet [30] is trained using events and frames as input, respectively. The results demonstrate that, despite event cameras effectively capturing dynamic semantics and filtering out redundant background information, event-based detectors exhibit inferior performance compared to their frame-based counterparts. This performance gap is attributed to the absence of crucial color and texture information for object detection. Given the complementary nature of events and frames, enhancing performance through their fusion is a viable approach. Hence, exploring effective fusion methods for events and frames is crucial. In this work, we propose CAFR to effectively leverage the complementary information from events and frames. Integrating our CAFR

Table 2: Ablation study on key components. This table compares key components of the CAFR: “Mul&Add” (multiplication and addition operations), “CrossAtt” (cross-self-attention), and “Branch” (module implementation branch). The bold value indicates the highest score.

Mul&Add	CrossAtt	FR	Branch	mAP_{50} (%)	mAP (%)
✓			Both	84.3	41.5
	✓		Both	84.2	42.2
		✓	Both	84.4	43.6
✓	✓		Both	82.7	42.4
✓		✓	Both	83.0	43.2
	✓	✓	Both	86.1	45.3
✓	✓	✓	(a)	86.3	44.7
✓	✓	✓	(b)	83.5	42.1
✓	✓	✓	Both	86.7	46.0

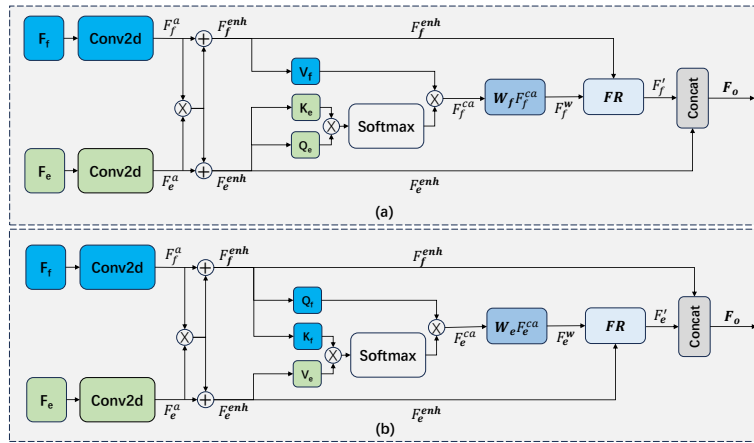


Fig. 5: Different network architecture designs for the fusion module. It includes: (a) a single branch consisting of only frame-dominated CrossAtt and FR; and (b) a single branch consisting of only event-dominated CrossAtt and FR.

modules into RetinaNet, the performance can be significantly improved by **4%** and **13%** on the PKU-DDD17-Car dataset and DSEC dataset, respectively.

Effectiveness of each key component of CAFR. To further investigate the impact of different components on object detection, we train our model with varying network settings on the PKU-DDD17-Car dataset using events and frames as input. As shown in Tab. 2, the experimental results demonstrate that combining all components, Mul&Add, CrossAtt, and FR, achieves the best detection performance.

Multi-branch vs. single-branch. We further explore the effect of retaining only one network branch in CAFR. The different network architecture designs

Table 3: Comparison with SOTA methods on the DSEC dataset.

Modality	Method	Model type	mAP (%)			
			Car	Pedestrian	Large vehicle	Average
Events + Frames	SENet [20]	Attention	38.4	14.9	26.0	26.2
	ECANet [49]		36.7	12.8	27.5	25.7
	CBAM [50]		37.7	13.5	27.0	26.1
	SAGate [11]	RGB-D	32.5	10.4	16.0	19.6
	DCF [23]		36.3	12.7	28.0	25.7
	SPNet [57]		39.2	17.8	26.2	27.7
	FPN-Fusion [48]	RGB-E	37.5	10.9	24.9	24.4
	DRFuser [38]		38.6	15.1	30.6	28.1
	RAMNet [15]		24.4	10.8	17.6	17.6
	CMX [55]		41.6	16.4	29.4	29.1
	FAGC [5]		39.8	14.4	33.6	29.3
	RENet [58]		40.5	17.2	30.6	29.4
	EFNet [46]		41.1	15.8	32.6	30.0
	CAFR (Ours)		49.9	25.8	38.2	38.0

are illustrated in Fig. 5. In this figure, (a) and (b) represent a single branch consisting of only frame-dominated CrossAtt and FR and a single branch consisting of only event-dominated CrossAtt and FR, respectively. The results in Tab. 2 demonstrate that the dual network branch (as depicted in Fig. 4) achieves superior performance compared to using a single network branch. This suggests that both the event-based branch and the frame-based branch are important.

4.4 Comparison with SOTA Methods

We conduct a comprehensive evaluation by comparing our method with SOTA methods on both the DSEC dataset and the PKU-DDD17-Car dataset. Additionally, we thoroughly analyze the robustness of our method, particularly its effectiveness in handling corrupted data. The results showcase the strengths of our approach, demonstrating excellent performance and notable robustness in challenging scenarios. We delve into the specific details in the following:

Comparison with SOTA methods on the DSEC dataset. To the best of our knowledge, there is limited research on RGB-event fusion methods specifically applied to the DSEC dataset. To address this gap, we replace our proposed fusion modules with SOTA alternatives from both the RGB-Event domain, including FPN-Fusion [48], DRFuser [38], RAMNet [15], CMX [55], FAGC [5], RENet [58], and EFNet [46], and the RGB-D domain, comprising SAGate [33], DCF [23], and SPNet [57]. Additionally, we compare our method with well-known attention modules such as SENet [20], ECANet [49], and CBAM [50]. We maintain consistency in event representation (voxel grid), network structure (RetinaNet), loss, and hyperparameter settings across all comparative experiments, with the only variation being the fusion module. The experimental results

Table 4: Comparison with SOTA methods on the PKU-DDD17-Car dataset.

Modality	Method	Input representation	Model type	mAP_{50} (%)	mAP (%)
Events	MTC [8]	Channel image	Events only	47.8	-
	ASTMNet [28]	Event embedding		46.2	-
Frames	SSD [34]	Frame	Frames only	73.1	-
	Faster-RCNN [43]			80.2	-
	YOLOv4 [2]			81.3	-
Events + Frames	SENet [20]	Voxel grid + Frame	Attention	81.6	42.4
	ECANet [49]			82.2	40.8
	CBAM [50]			81.9	42.8
	SAGate [11]	Voxel grid + Frame	RGB-D	82.0	43.4
	DCF [23]			83.4	42.5
	SPNet [57]			84.7	43.3
	JDF [27]	Channel image + Frame	RGB-E	84.1	-
	FPN-Fusion [48]	Voxel grid + Frame		81.9	41.6
	DRFuser [38]	Voxel grid + Frame		82.6	42.4
	RAMNet [15]	Voxel grid + Frame		79.6	38.8
CMX [55]	Voxel grid + Frame	80.4		39.0	
FAGC [5]	Voxel grid + Frame	84.8		42.4	
RENet [58]	Voxel grid + Frame	81.4		43.9	
EFNet [46]	Voxel grid + Frame	83.0		41.6	
CAFR (Ours)	Voxel grid + Frame	86.7		46.0	

are summarized in Tab. 3. Compared with other methods, our CAFR achieves significant improvements. Notably, CAFR outperforms the second-best method, EFNet [46], by an impressive margin of **8.0%**.

Comparison with SOTA methods on the PKU-DDD17-Car dataset. Several works [5, 27, 28] have been conducted on the PKU-DDD17-Car dataset. Similar to DSEC, we compare our method with SOTA alternatives from the RGB-Event domain, the RGB-D domain, and attention modules. The results are listed in Tab. 4. It is evident that frame-based detectors outperform event-based detectors due to the crucial color and texture information lacking in event data. Compared with single-modal methods, fusion-based methods perform better. In particular, our CAFR consistently improves performance on both the DSEC dataset and the PKU-DDD17-Car dataset, showcasing its excellent generalization ability. Our CAFR achieves the best performance in terms of mAP_{50} and mAP with accuracy of 86.7% and 46.0%, respectively. We also visualize the detection results in challenging scenarios (See in **Supplemental Material**).

Robustness. In this experiment, we assess the model’s robustness using our generated corruption data. All models undergo training with clean data and subsequent testing on the corrupted data. The corrupted data encompasses 15 diverse corruption types, as detailed earlier, broadly categorized into four groups: noise, blur, weather, and digital. Robustness evaluations are conducted across five severity levels, ranging from 1 to 5, for each corruption type. The comprehensive results are presented in Tab. 5. Compared to single-modal input using frames only, the fusion of events and frames leads to a substantial improvement in the

Table 5: The performance of different methods under various corruption conditions, including noise, blur, weather, and digital.

Method	Model type	$mPC_{50}(\%)$				
		Average	Noise	Blur	Weather	Digital
Frames only [30]	Frames only	38.7	47.6	25.3	28.5	53.0
SENet [20]	Attention	63.6	68.6	56.6	58.9	70.3
ECANet [49]		67.1	72.6	57.6	66.8	71.4
CBAM [50]		65.2	69.9	57.2	62.4	70.3
SAGate [11]	RGB-D	63.6	68.1	55.9	61.1	69.4
DCF [23]		65.7	70.9	57.9	62.9	71.1
SPNet [57]		66.6	70.6	58.7	64.8	72.3
FPN-Fusion [48]	RGB-E	64.7	70.0	56.6	63.9	69.4
DRFuser [38]		67.7	72.1	59.4	67.8	71.4
RAMNet [15]		53.9	53.5	43.3	54.3	64.6
CMX [55]		64.2	67.7	56.0	62.9	70.2
FAGC [5]		52.4	62.8	38.5	48.4	59.9
RENet [58]		57.2	58.5	72.3	29.9	68.1
EFNet [46]		66.4	67.1	58.2	66.7	73.4
CAFR (Ours)		69.5	73.6	57.0	70.6	76.7

model’s robustness. For instance, our CAFR exhibits significantly better robustness (**69.5%** versus **38.7%**) compared to using frames only. In comparison to other fusion methods, our proposed CAFR demonstrates superior performance. These findings highlight the effectiveness of CAFR in strengthening the model against corrupted data across diverse severity levels and types.

5 Conclusion

This paper proposes a novel hierarchical feature refinement network for event-frame fusion. The key idea is the coarse-to-fine fusion module, named the cross-modality adaptive feature refinement module (CAFR). The CAFR employs attention mechanisms and feature statistics to enhance feature representations at the feature level. Extensive experiments are conducted on two datasets: the low-resolution PKU-DDD17-Car dataset and the high-resolution DSEC dataset. The results consistently demonstrate performance improvements on both datasets, showcasing the method’s effectiveness and strong generalization. Furthermore, the model’s robustness is thoroughly evaluated on generated corruption data, revealing superior robustness compared to other SOTA methods. These findings highlight the effectiveness of the proposed CAFR in strengthening the model across diverse scenarios and datasets.

Acknowledgments: This work is supported by the MANNHEIM-CeCaS (Central Car Server – Supercomputing for Automotive, No. 5310032), in part by Na-

tional Natural Science Foundation of China (No. 62372329), in part by Shanghai Scientific Innovation Foundation (No.23DZ1203400), in part by Shanghai Rising Star Program (No.21QC1400900), in part by Tongji-Qomolo Autonomous Driving Commercial Vehicle Joint Lab Project, and in part by Xiaomi Young Talents Program.

References

1. Binas, J., Neil, D., Liu, S., Delbrück, T.: DDD17: end-to-end DAVIS driving dataset. *CoRR* (2017)
2. Bochkovskiy, A., Wang, C.Y., Liao, H.Y.M.: Yolov4: Optimal speed and accuracy of object detection. *arXiv preprint* (2020)
3. Brandli, C., Berner, R., Yang, M., Liu, S.C., Delbruck, T.: A 240×180 130 db $3 \mu\text{s}$ latency global shutter spatiotemporal vision sensor. *IEEE Journal of Solid-State Circuits* **49**(10), 2333–2341 (2014)
4. Cao, H., Chen, G., Li, Z., Hu, Y., Knoll, A.: Neurograsp: multimodal neural network with euler region regression for neuromorphic vision-based grasp pose estimation. *IEEE Transactions on Instrumentation and Measurement* **71**, 1–11 (2022)
5. Cao, H., Chen, G., Xia, J., Zhuang, G., Knoll, A.: Fusion-based feature attention gate component for vehicle detection based on event camera. *IEEE Sensors Journal* **21**(21), 24540–24548 (2021)
6. Cao, H., Chen, G., Zhao, H., Jiang, D., Zhang, X., Tian, Q., Knoll, A.: Sdpt: Semantic-aware dimension-pooling transformer for image segmentation. *IEEE Transactions on Intelligent Transportation Systems* pp. 1–13 (2024)
7. Chen, G., Cao, H., Conradt, J., Tang, H., Rohrbein, F., Knoll, A.: Event-based neuromorphic vision for autonomous driving: A paradigm shift for bio-inspired visual sensing and perception. *IEEE Signal Processing Magazine* **37**(4), 34–49 (2020)
8. Chen, G., Cao, H., Ye, C., Zhang, Z., Liu, X., Mo, X., Qu, Z., Conradt, J., Röhrbein, F., Knoll, A.: Multi-cue event information fusion for pedestrian detection with neuromorphic vision sensors. *Frontiers in Neurorobotics* **13**, 10 (2019)
9. Chen, G., Chen, K., Zhang, L., Zhang, L., Knoll, A.: Vcanet: Vanishing-point-guided context-aware network for small road object detection. *Automotive Innovation* **4**, 400–412 (2021)
10. Chen, N.F.Y.: Pseudo-labels for supervised learning on dynamic vision sensor data, applied to object detection under ego-motion. In: *CVPRW* (2018)
11. Chen, X., Lin, K.Y., Wang, J., Wu, W., Qian, C., Li, H., Zeng, G.: Bi-directional cross-modality feature propagation with separation-and-aggregation gate for rgb-d semantic segmentation. In: *ECCV* (2020)
12. Dodge, S., Karam, L.: Understanding how image quality affects deep neural networks. In: *QoMEX* (2016)
13. Fu, K., Fan, D.P., Ji, G.P., Zhao, Q.: JI-dcf: Joint learning and densely-cooperative fusion framework for rgb-d salient object detection. In: *CVPR* (2020)
14. Gallego, G., Delbrück, T., Orchard, G., Bartolozzi, C., Taba, B., Censi, A., Leutenegger, S., Davison, A.J., Conradt, J., Daniilidis, K., et al.: Event-based vision: A survey. *IEEE transactions on pattern analysis and machine intelligence* **44**(1), 154–180 (2020)
15. Gehrig, D., Rüegg, M., Gehrig, M., Hidalgo-Carrió, J., Scaramuzza, D.: Combining events and frames using recurrent asynchronous multimodal networks for monocular depth prediction. *IEEE Robotics and Automation Letters* **6**(2), 2822–2829 (2021)

16. Gehrig, M., Aarents, W., Gehrig, D., Scaramuzza, D.: Dsec: A stereo event camera dataset for driving scenarios. *IEEE Robotics and Automation Letters* **6**(3), 4947–4954 (2021)
17. Gehrig, M., Scaramuzza, D.: Recurrent vision transformers for object detection with event cameras. In: *CVPR* (2023)
18. He, K., Zhang, X., Ren, S., Sun, J.: Deep residual learning for image recognition. In: *CVPR* (2016)
19. Hendrycks, D., Dietterich, T.: Benchmarking neural network robustness to common corruptions and perturbations. *arXiv preprint* (2019)
20. Hu, J., Shen, L., Sun, G.: Squeeze-and-excitation networks. In: *CVPR* (2018)
21. Hu, Y., Delbruck, T., Liu, S.C.: Learning to exploit multiple vision modalities by using grafted networks. In: *ECCV* (2020)
22. Huang, X., Belongie, S.: Arbitrary style transfer in real-time with adaptive instance normalization. In: *ICCV* (2017)
23. Ji, W., Li, J., Yu, S., Zhang, M., Piao, Y., Yao, S., Bi, Q., Ma, K., Zheng, Y., Lu, H., et al.: Calibrated rgb-d salient object detection. In: *CVPR* (2021)
24. Jiang, Z., Xia, P., Huang, K., Stechele, W., Chen, G., Bing, Z., Knoll, A.: Mixed frame-/event-driven fast pedestrian detection. In: *ICRA* (2019)
25. Jocher, G., Stoken, A., Borovec, J., Changyu, L., Hogan, A., Diaconu, L., Ingham, F., Poznanski, J., Fang, J., Yu, L.U.: Yolov5: V3. 1-bug fixes and performance improvements. *Zenodo* (2020)
26. Kingma, D.P., Ba, J.: Adam: A method for stochastic optimization. *arXiv preprint* (2014)
27. Li, J., Dong, S., Yu, Z., Tian, Y., Huang, T.: Event-based vision enhanced: A joint detection framework in autonomous driving. In: *ICME* (2019)
28. Li, J., Li, J., Zhu, L., Xiang, X., Huang, T., Tian, Y.: Asynchronous spatio-temporal memory network for continuous event-based object detection. *IEEE Transactions on Image Processing* **31**, 2975–2987 (2022)
29. Lin, T.Y., Dollár, P., Girshick, R., He, K., Hariharan, B., Belongie, S.: Feature pyramid networks for object detection. In: *CVPR* (2017)
30. Lin, T.Y., Goyal, P., Girshick, R., He, K., Dollár, P.: Focal loss for dense object detection. In: *ICCV* (2017)
31. Lin, T.Y., Maire, M., Belongie, S., Hays, J., Perona, P., Ramanan, D., Dollár, P., Zitnick, C.L.: Microsoft coco: Common objects in context. In: Fleet, D., Pajdla, T., Schiele, B., Tuytelaars, T. (eds.) *ECCV* (2014)
32. Liu, L., Ouyang, W., Wang, X., Fieguth, P., Chen, J., Liu, X., Pietikäinen, M.: Deep learning for generic object detection: A survey. *International journal of computer vision* **128**, 261–318 (2020)
33. Liu, M., Qi, N., Shi, Y., Yin, B.: An attention fusion network for event-based vehicle object detection. In: *ICIP* (2021)
34. Liu, W., Anguelov, D., Erhan, D., Szegedy, C., Reed, S., Fu, C.Y., Berg, A.C.: SSD: Single shot multibox detector. In: *ECCV* (2016)
35. Luo, A., Li, X., Yang, F., Jiao, Z., Cheng, H., Lyu, S.: Cascade graph neural networks for rgb-d salient object detection. In: *ECCV* (2020)
36. Michaelis, C., Mitzkus, B., Geirhos, R., Rusak, E., Bringmann, O., Ecker, A.S., Bethge, M., Brendel, W.: Benchmarking robustness in object detection: Autonomous driving when winter is coming. *arXiv preprint* (2019)
37. Moeys, D.P., Corradi, F., Li, C., Bamford, S.A., Longinotti, L., Voigt, F.F., Berry, S., Taverni, G., Helmchen, F., Delbruck, T.: A sensitive dynamic and active pixel vision sensor for color or neural imaging applications. *IEEE transactions on biomedical circuits and systems* **12**(1), 123–136 (2017)

38. Munir, F., Azam, S., Yow, K.C., Lee, B.G., Jeon, M.: Multimodal fusion for sensorimotor control in steering angle prediction. *Engineering Applications of Artificial Intelligence* **126**, 107087 (2023)
39. Oksuz, K., Cam, B.C., Kalkan, S., Akbas, E.: Imbalance problems in object detection: A review. *IEEE transactions on pattern analysis and machine intelligence* **43**(10), 3388–3415 (2020)
40. Paszke, A., Gross, S., Massa, F., Lerer, A., Bradbury, J., Chanan, G., Killeen, T., Lin, Z., Gimelshein, N., Antiga, L., et al.: Pytorch: An imperative style, high-performance deep learning library. *NeurIPS* **32** (2019)
41. Perot, E., De Tournemire, P., Nitti, D., Masci, J., Sironi, A.: Learning to detect objects with a 1 megapixel event camera. *NeurIPS* (2020)
42. Redmon, J., Divvala, S., Girshick, R., Farhadi, A.: You only look once: Unified, real-time object detection. In: *CVPR* (2016)
43. Ren, S., He, K., Girshick, R., Sun, J.: Faster r-cnn: Towards real-time object detection with region proposal networks. *IEEE transactions on pattern analysis and machine intelligence* **39**(6), 1137–1149 (2017)
44. Seichter, D., Köhler, M., Lewandowski, B., Wengefeld, T., Gross, H.M.: Efficient rgb-d semantic segmentation for indoor scene analysis. In: *ICRA* (2021)
45. Sun, K., Wu, W., Liu, T., Yang, S., Wang, Q., Zhou, Q., Ye, Z., Qian, C.: Fab: A robust facial landmark detection framework for motion-blurred videos. In: *ICCV* (2019)
46. Sun, L., Sakaridis, C., Liang, J., Jiang, Q., Yang, K., Sun, P., Ye, Y., Wang, K., Van Gool, L.: Event-based fusion for motion deblurring with cross-modal attention. In: *ECCV* (2022)
47. Sun, P., Zhang, W., Wang, H., Li, S., Li, X.: Deep rgb-d saliency detection with depth-sensitive attention and automatic multi-modal fusion. In: *CVPR* (2021)
48. Tomy, A., Paigwar, A., Mann, K.S., Renzaglia, A., Laugier, C.: Fusing event-based and rgb camera for robust object detection in adverse conditions. In: *ICRA* (2022)
49. Wang, Q., Wu, B., Zhu, P., Li, P., Zuo, W., Hu, Q.: Eca-net: Efficient channel attention for deep convolutional neural networks. In: *CVPR* (2020)
50. Woo, S., Park, J., Lee, J.Y., Kweon, I.S.: Cbam: Convolutional block attention module. In: *ECCV* (2018)
51. Xia, Y., Gladkova, M., Wang, R., Li, Q., Stilla, U., Henriques, J.F., Cremers, D.: Casspr: Cross attention single scan place recognition. In: *ICCV* (2023)
52. Xia, Y., Xu, Y., Li, S., Wang, R., Du, J., Cremers, D., Stilla, U.: Soe-net: A self-attention and orientation encoding network for point cloud based place recognition. In: *CVPR* (2021)
53. Xie, B., Deng, Y., Shao, Z., Li, Y.: Eisnet: A multi-modal fusion network for semantic segmentation with events and images. *IEEE Transactions on Multimedia* pp. 1–12 (2024)
54. Ying, X., Chuah, M.C.: Uctnet: Uncertainty-aware cross-modal transformer network for indoor rgb-d semantic segmentation. In: *ECCV* (2022)
55. Zhang, J., Liu, H., Yang, K., Hu, X., Liu, R., Stiefelhagen, R.: Cmx: Cross-modal fusion for rgb-x semantic segmentation with transformers. *IEEE Transactions on Intelligent Transportation Systems* **24**(12), 14679–14694 (2023)
56. Zhang, Q., Zhao, S., Luo, Y., Zhang, D., Huang, N., Han, J.: Abmdrnet: Adaptive-weighted bi-directional modality difference reduction network for rgb-t semantic segmentation. In: *CVPR* (2021)
57. Zhou, T., Fu, H., Chen, G., Zhou, Y., Fan, D.P., Shao, L.: Specificity-preserving rgb-d saliency detection. In: *ICCV* (2021)

58. Zhou, Z., Wu, Z., Boutteau, R., Yang, F., Demonceaux, C., Ginhac, D.: Rgb-event fusion for moving object detection in autonomous driving. In: ICRA (2023)
59. Zhu, A.Z., Yuan, L., Chaney, K., Daniilidis, K.: Unsupervised event-based learning of optical flow, depth, and egomotion. In: CVPR (2019)

A More Experimental Details

A.1 Datasets

DDD17. The vehicles in the DDD17 dataset were manually labeled by the authors of [27] to create the PKU-DDD17-Car dataset for object detection tasks. Additional details about the PKU-DDD17-Car dataset are outlined in Tab. 6.

DSEC. The original dataset comprises 53 sequences captured in three distinct regions of Switzerland. RGB frames are captured using the FLIR color camera, which boasts a resolution of 1440×1080 . The original DSEC dataset [16] lacks the required labels for object detection. The labels introduced in [48] is used in this work. This annotated dataset consists of a total of 41 sequences, allocated for training (33 sequences), validation (3 sequences), and testing (5 sequences). Notably, the dataset covers a wide range of lighting conditions, from ideal to highly challenging. This diversity guarantees comprehensive testing of vision systems, ensuring their robustness and applicability in real-world settings. Additionally, unlike the DDD17 dataset, in which both event data and RGB data are sourced from the same DAVIS camera, the raw event data and RGB data in the DSEC dataset are not aligned; they do not correspond to the same frame. Therefore, additional preprocessing of the raw DSEC data is essential. Further details regarding the preprocessing steps are provided below:

Homographic transformation. To address the misalignment between the event data and RGB data, the two types of data need to be transformed into the same frame. The dataset provides a baseline of 4.5 cm between the two cameras, allowing for the transformation to a common viewpoint. In our pre-processing, we leverage the homographic transformation induced by pure rotation, as derived in Eq. 13, to align the scene from an RGB frame to an event-camera frame. It’s important to note that, in our scenario, the scene appears far away from the camera, and the baseline of 4.5 cm is smaller than the distances of the scene objects.

$$P_{\text{event,rgb}} = K_{\text{event}} * R_{\text{rgb}} * R_{\text{event,rgb}} * R_{\text{event}}^T * K_{\text{rgb}}^{-1}. \quad (13)$$

where K_{rgb} and K_{event} represent the intrinsic camera matrices of the RGB and event cameras, respectively. Similarly, R_{rgb} and R_{event} denote the rotation matrices accounting for the transition from distorted to undistorted frames for each camera. Additionally, $R_{\text{event,rgb}}$ stands for the rotation matrix aligning the RGB camera coordinate system with that of the event camera.

Fig. 6 illustrates the impact of the homomorphic transformation. In the left figure, the RGB image and the event image are not aligned. However, after applying the homomorphic transformation, the RGB image and the event image become aligned, sharing the same frame and being suitable for multimodal fusion. Additionally, the size of the RGB images is resized to match the event image, ensuring that both types of data have the same field of view and resolution.

Annotation generation. To facilitate object detection on the DSEC dataset, we employed simulated annotations provided by [48]. YOLOv5 [25] was used

Table 6: A detailed description of the recorded data in the PKU-DDD17-CAR dataset

Recorded data (.hdf5)	Condition	Length (s)	Type
1487339175	day	347	test
1487417411	day	2096	test
1487419513	day	1976	train
1487424147	day	3040	train
1487430438	day	3135	train
1487433587	night-fall	2335	train
1487593224	day	524	test
1487594667	day	2985	train
1487597945	night-fall	50	test
1487598202	day	1882	train
1487600962	day	2143	test
1487608147	night-fall	1208	train
1487609463	night-fall	101	test
1487781509	night-fall	127	test

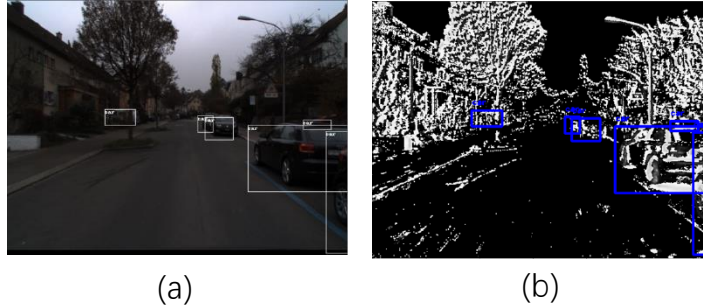
**Fig. 6:** Examples illustrate the comparison before and after the homomorphic transformation. On the left (a): an overlay map of the original RGB image and event image. On the right (b): an overlay map of the RGB image and event image after the homomorphic transformation.**Table 7:** Object annotations in the labeled DSEC dataset.

Categories	Car	Pedestrian	Large vehicle (Bus & Truck)
Count	100068	17126	14771
Percentage	0.76	0.13	0.11

to label RGB images. The homographic transformation was applied to transfer labels from RGB images to the event frame, accounting for objects within the event camera’s 640×480 resolution. Examples of labeled events and RGB images are depicted in Fig. 7, encompassing three object classes: car, pedestrian, and large vehicle (refer to Tab. 7).

Table 8: Data amount in the labeled DSEC dataset.

Type	Train	Val	Test	Total
Sequences	33	3	5	41
Frames	44148	3642	4896	52686

**Fig. 7:** Examples of events and RGB images with annotations. Left (a): RGB image; Right (b): event frame.**Table 9:** The details of different corruption types.

Group	Corruption Type
Noise	Gaussian Noise, Shot Noise, Impulse Noise
Blur	Defocus Blur, Glass Blur, Motion Blur, Zoom Blur
Weather	Fog, Snow, Frost, Brightness
Digital	Contrast, Elastic Transform, Pixelate, Jpeg Compression

After the aforementioned pre-processing steps, we acquired the labeled DSEC dataset for experimentation. The dataset comprises a total of 41 sequences, with 33 sequences allocated for training, 3 sequences for validation, and the remaining 5 sequences designated for testing. Detailed information about the data is presented in Tab. 8, where the event data file is approximately 300 GB and the RGB data file is around 23 GB.

Corruption data. In this work, we introduced 15 types of corruption, each with five levels of severity, to assess the impact of diverse corruption types on object detection models. The chosen corruption types are categorized into four groups: noise, blur, weather, and digital. The specific corruption types are detailed in Tab. 9. Fig. 8 provides an illustration of these corruption types at severity level 2. All corruption treatments are applied to the test set, enabling us to evaluate a model’s robustness against previously unseen corruptions.

Noise. The first corruption type is Gaussian noise. This corruption may occur in low-light conditions. Electronic noise caused by the discontinuous character

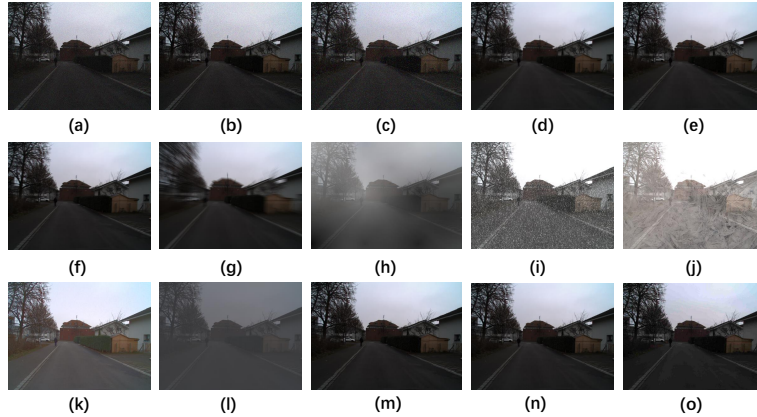


Fig. 8: The dataset encompasses 15 types of algorithmically generated corruptions, categorized into noise, blur, weather, and digital groups. The corrupted images, denoted from (a) to (o), include Gaussian Noise, Shot Noise, Impulse Noise, Defocus Blur, Glass Blur, Motion Blur, Zoom Blur, Fog, Snow, Frost, Brightness, Contrast, Elastic Transform, Pixelate, and Jpeg Compression. Each corruption type exhibits five severity levels, resulting in a total of 75 distinct corruptions. The images presented here correspond to severity level 2.

of light is known as shot noise, also referred to as poisson noise. Impulse noise is the color analog of salt-and-pepper noise and can be caused by bit errors.

Blur. Defocus blur occurs when the image is out of focus. Glass blur appears on "frosted glass" windows or panels. When the camera is moving swiftly, motion blur happens. When the camera advances quickly toward an item, zoom blur occurs.

Weather. Snow is a type of precipitation that impairs vision. When there are ice crystals on the lenses or windows, frost occurs. A diamond-square method is used to render the fog that surrounds the items. The brightness varies with the intensity of daylight.

Digital. Based on the lighting and the subject's color, contrast can be either high or low. The elastic transform enlarges or reduces picture regions. Pixelate occurs when upsampling low-resolution images. Jpeg compression is a lossy image compression format that produces compression artifacts.

A.2 Training details.

Our model is implemented using PyTorch [40], and we initialize the event-based and frame-based backbone branches with pre-trained ResNet-50 [18]. The input data for the PKU-DDD17-Car dataset and DSEC dataset are resized to 346×260 and 640×480 , respectively. Furthermore, we train the model using the Adam optimizer [26] with an initial learning rate of 1×10^{-4} . The experiments are

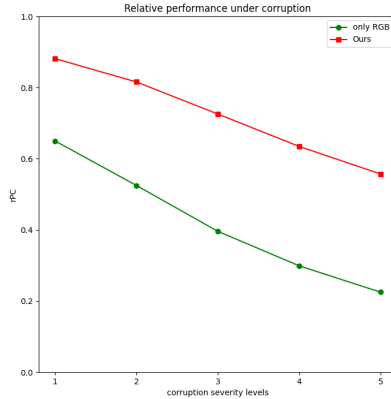


Fig. 9: Relative performance under various severity.

carried out on an Nvidia RTX 3090 GPU with a system running Ubuntu 20.04. During training, the input from the RGB image is set to blank (zero) with a 15% probability. This strategy compels the sensor fusion model to extract information primarily from the second modality, the event camera, thereby enhancing the model’s robustness against corruption in the frame-based camera. The total number of epochs is set to 200, with a batch size of 8 for the PKU-DDD17-Car dataset and 1 for the DSEC dataset, respectively.

B More Experimental Analysis

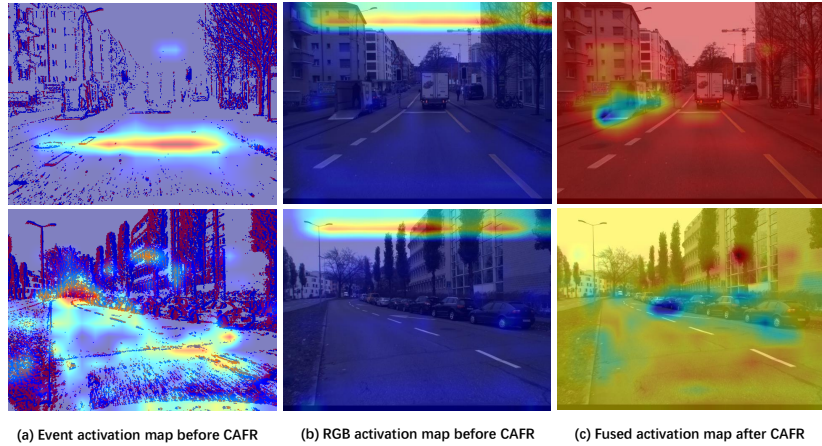
Performance under different lighting conditions. To analyze the contribution of the event camera, we assess the performance gain under different illumination conditions. Detailed comparisons are provided in Tab. 10. The results illustrate that our proposed CAFR, capitalizing on the complementary nature of events and frames, consistently improves detection performance and is better than other fusion methods across various lighting conditions. This analysis provides valuable insights into the effectiveness of incorporating event data in improving overall model performance under diverse illumination scenarios.

Efficiency analysis. As detailed in Tab. 10, the running speeds of various methods are presented. In comparison with other fusion methods, such as CBAM [50], SAGate [11], and RENet [58], the proposed method exhibits comparable running speed while significantly enhancing detection accuracy.

More robustness analysis. Fig. 9 illustrates the relative performance under corruption (RPC) at severity levels ranging from 1 to 5. Across all models, there is a consistent decline in relative performance as the severity of corruption increases. Notably, the model relying solely on RGB data exhibits the steepest

Table 10: Comparison with SOTA fusion alternatives: COCO mAP@0.50:0.95 on the PKUDDDD17-CAR dataset for the different methods.

Method	Model type	Test(All day)	Test(Day)	Test(Night)	FPS
SENet [20]	Attention	42.4	43.7	37.0	8.0
ECA [49]		40.8	42.2	36.1	7.6
CBAM [50]		42.8	44.2	38.0	10.3
SAGate [11]	RGB-D	43.4	44.9	38.0	11.8
DCF [23]		42.5	43.4	39.0	13.8
SPNet [57]		43.3	44.9	37.1	9.1
FPN-Fusion [48]	RGB-E	41.6	43.2	35.7	12.0
DRFuser [38]		42.4	43.3	38.8	11.5
RAMNet [15]		38.8	39.2	36.9	11.5
CMX [55]		39.0	40.2	35.4	2.8
FAGC [5]		42.4	43.7	36.7	5.3
RENet [58]		43.9	45.4	39.1	5.0
EFNet [46]		41.6	43.4	35.1	9.7
CAFR (Ours)		46.0	46.9	42.1	6.4

**Fig. 10:** Representative examples of different activation maps on the DSEC dataset are: (a) event activation map before CAFR; (b) RGB activation map before CAFR; and (c) fused activation map after CAFR.

decline, indicating its lower robustness. In contrast, the proposed fusion method significantly improves robustness across different severity levels.

Visualization of activation maps. In the fig. 10, we visualize the activation maps of RGB and event modalities before and after CAFR. After applying CAFR, the model demonstrates enhanced focus on significant regions.

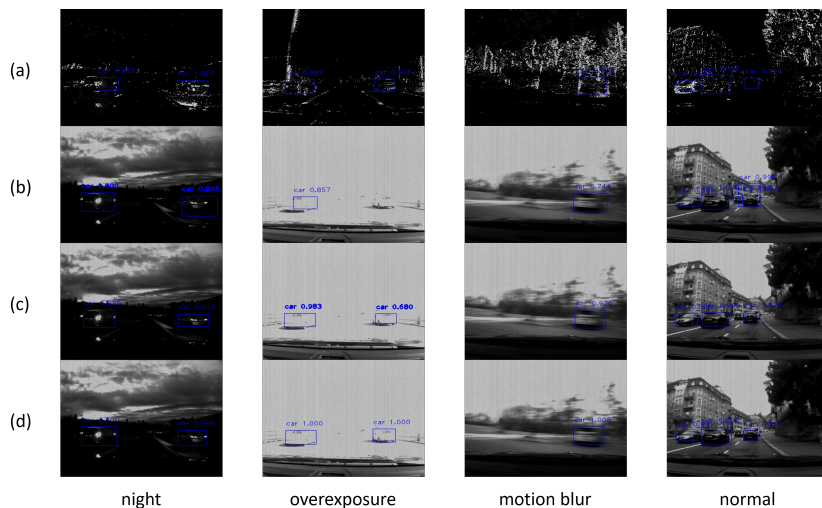


Fig. 11: Representative examples of different object detection results on the PKU-DDD17-Car dataset: (a) our baseline using event images; (b) our baseline using frames; (c) SPNet [57] (the second-best model in terms of $mAP_{50}\%$ and $mAP\%$) using frames and events. (d) our method using frames and events.

Results on detection predictions. In Fig. 11 and Fig. 12, we visualize the detection results selected from the PKU-DDD17-Car dataset and DSEC dataset, respectively. The results demonstrate that the proposed method can consistently produce satisfactory detection results in various challenging scenarios. Compared with the second-best methods, SPNet [57] and EFNet [46], our method performs better prediction results.

C Limitations

While our CAFR has demonstrated efficacy in the context of object detection, it is essential to acknowledge a current limitation. The scope of our evaluations has been confined to this specific task, and extrapolating the performance of CAFR to other prevalent perception tasks, such as semantic segmentation, depth prediction, and steering angle prediction, remains unexplored. Future investigations could delve into the broader applicability of CAFR, providing insights into its adaptability and potential limitations across diverse perception domains.

D More Related Works

In other areas of cross-modal fusion, such as depth, thermal, and event data, we discuss relevant works below. In the field of RGB-D salient object detection (SOD), the joint learning and densely cooperative fusion framework introduced

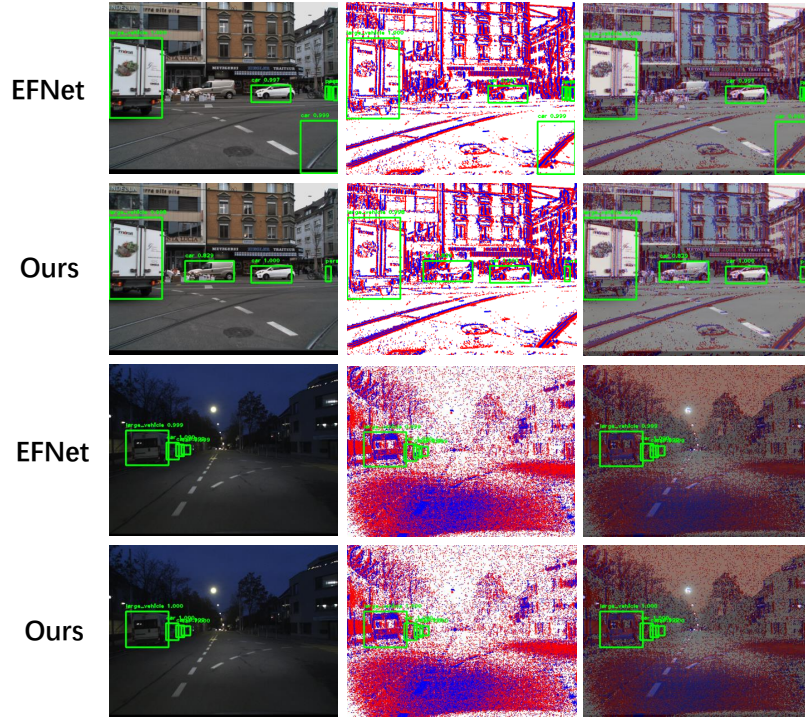


Fig. 12: Representative examples of different object detection results on the DSEC dataset. The first two rows are daytime scenes, and the last two rows are nighttime scenes. Each column represents RGB images, event frames, and merged RGB event frames, respectively.

in [13] aims to improve performance. The authors of [35] developed graph-based techniques to design network architectures for RGB-D SOD. Additionally, an automatic architecture search approach for RGB-D SOD is presented in [47]. For semantic segmentation, the authors of [44] proposed the efficient scene analysis network (ESANet) for RGB-D semantic segmentation, utilizing channel attention [20] for RGB-D fusion. Furthermore, an uncertainty-aware self-attention mechanism is employed in [54] for indoor RGB-D semantic segmentation. The adaptive-weighted bi-directional modality difference reduction network proposed in [56] addresses RGB-T semantic segmentation. Recently, a multi-modal fusion network (EISNet) introduced in [53] aims to enhance semantic segmentation performance using events and images.